Journal of Power Sources 197 (2012) 1–11

Contents lists available at SciVerse ScienceDirect

Journal of Power Sources

journal homepage: www.elsevier.com/locate/jpowsour

Assessing porosity of proton exchange membrane fuel cell gas diffusion layers by scanning electron microscope image analysis

Johnathon Farmer[a,*], Binh Duong[a], Supapan Seraphin[a], Sirivatch Shimpalee[b], Michael J. Martínez-Rodríguez[b], John W. Van Zee[b]

[a] Department of Materials Science and Engineering, The University of Arizona, Tucson, AZ 85721, United States
[b] Department of Chemical Engineering, The University of South Carolina, Columbia, SC 29208, United States

ARTICLE INFO

Article history:
Received 17 May 2011
Received in revised form 14 August 2011
Accepted 15 August 2011
Available online 22 August 2011

Keywords:
Porosity
PEM fuel cell
Gas diffusion layer
SEM
Image analysis
Micro porous layer

ABSTRACT

A gas diffusion layer (GDL) in a proton exchange membrane fuel cell may consist of several, materials of different porosities, with each material serving a specific set of functions. For example, samples analyzed in this work consisted of a macro porous carbon paper substrate treated with a, hydrophobic wet proofing material in differing amounts, which was then coupled to a micro porous, layer. The porosities of four such GDLs were determined by using 2D scanning electron microscope (SEM) images to mathematically model the volumes filled by each solid in the 3D structures. Results, were then compared with mercury intrusion porosimetry (MIP) measurements to verify the accuracy, of the method. It was found that the use of SEM not only allowed for detailed porosity analysis of, separate porous materials within the GDL, but also porosity for the entire GDL could be calculated for, the seemingly complex structures with reasonable accuracy. With some basic geometric assumptions, and use of the superposition principle, the calculated results were accurate to less than a 2% absolute, difference of the porosity measured by MIP for each of the four samples analyzed.

1. Introduction

In a proton exchange membrane fuel cell (PEMFC), the gas diffusion layer (GDL) plays several roles which impact the performance of the cell. Shimpalee et al. [1] state that a GDL is used to enhance the reaction area accessible to the reactants, while ensuring proper transport of product water, electrons, and heat of reaction. These processes are affected by properties of the GDL such as the porosity (ε) and tortuosity (τ). The porosity is defined as the volume ratio of void space in the material, while tortuosity is the ratio of the path length through the pores to the shortest linear distance between two points. Research has shown that these two properties relate the free stream diffusion coefficient (D_i) with the effective diffusion coefficient (D_{eff}) as expressed below:

$$D_{eff} = \frac{D_i}{f(\tau, \varepsilon)} \tag{1}$$

where the function $f(\tau, \varepsilon)$ is known as the MacMullin number [2].

The MacMullin number, N_M, is a dimensionless number that describes the resistance to flow through a porous media. The MacMullin number is more appropriately defined as:

$$N_M = f(\tau, \varepsilon) = \frac{\tau^n}{\varepsilon^m} \tag{2}$$

where n and m are empirical constants which differ depending on sample geometries. For a given type of sample, it has been shown that the tortuosity, and hence MacMullin number, can be expressed as a function of the porosity. The well known Bruggeman expression is:

$$N_M = \varepsilon^{-1.5} \tag{3}$$

which is found by empirical evidence [2,3] to hold true for carbon cloth GDLs. However, the Bruggeman expression has been found to underestimate the tortuosity [2,4] for carbon paper GDLs, such as those characterized in this study. For carbon paper GDLs, Martínez et al. [2] report that the MacMullin number more closely correlates to the porosity with:

$$N_M = \varepsilon^{-3.8} \tag{4}$$

Hence, knowledge of the predetermined relationship between porosity and MacMullin number for these GDLs allows for the calculation of resistance to diffusion that the porous membrane adds, by porosity alone.

* Corresponding author at: The University of Arizona, P.O. Box 210012, Tucson, AZ 85721-0012, United States. Tel.: +1 520 440 9564; fax: +1 520 621 8059.
E-mail addresses: jcfarmer@email.arizona.edu, farmer0192@yahoo.com (J. Farmer).

0378-7753/$ – see front matter © 2011 Elsevier B.V. All rights reserved.
doi:10.1016/j.jpowsour.2011.08.064

Nomenclature

ε	porosity
τ	tortuosity
D_i	free stream diffusion coefficient
D_{eff}	effective diffusion coefficient
N_M	MacMullin number
A_i	area hidden by a fiber intersection
d_f	fiber diameter
θ_i	angle of intersection
N	number of half layers
A_L	area hidden in a half layer by intersections with the fibers from the half layer directly above it
A_T	total area hidden in a half layer by intersections with the fibers from all half layers above it
A_C	cumulative area hidden in all half layers by intersections from fibers in all half layers above them

In this study, the porosity was determined the for several custom Toray carbon paper samples, using SEM and image processing. The samples used consisted of a macro porous carbon paper substrate and a micro porous layer (MPL), each treated with a different amount of wet-proofing material (WPM). Porosity determination by SEM image processing is common, but not for these types of samples. Most of the published techniques are tailored for samples of particulates, where the particle shapes are identified by image processing software such as in the method provided by Igathinathane et al. [5] or for samples with spherical pores where average pore radii are calculated as in the method provided by Diego et al. [6]. He et al. [7] performed porosity calculations on a Toray carbon paper substrate, but the sample did not have a micro porous layer, and the method provided only allowed for calculation of a 2D porosity. These single image methods were not suitable for the geometry of these custom samples, which had numerous material types and porosities on largely different scales. Images for two largely different samples are shown in Fig. 1. The carbon fiber substrate had pore dimensions on the order of 100 μm whereas the MPL had average pore dimensions on the order of 100 nm, making it impossible to accurately reflect both types of pores within a single image. Thus, a new method was needed to calculate the porosities for these samples.

The method developed for calculating porosity in this experiment is called the area per layer (APL) technique. This takes advantage of the good depth of field that a SEM provides in 2D images to make assumptions about the third dimension. The benefit of this is that the area of several layers of carbon fibers can be mostly seen in the same 2D image, where a layer has the thickness of a single carbon fiber which can be measured. By measuring the area fraction filled by different solids in the image with a known depth, one can calculate the volume fraction of solid after adjusting for volume hidden in the dimension normal to the plane of the image. This technique was applied to determine both the macro porosity of the treated carbon fiber substrate, and the micro porosity of the other materials, using separate images.

Results from MIP [8], were used to verify accuracy of the APL technique. MIP consists of applying pressure to a sample immersed in mercury (a nonwetting fluid) to force fluid into the pores. Measurements of the applied pressure and the volume of mercury intruded into the pores are used to determine the pore size and porosity of the sample. As larger pressures are required to force mercury into smaller pores, a pore size distribution in the sample can be associated with the pressures needed to achieve intrusion, assuming pressures are accurately monitored during the porosimetry process. However, the reliability of MIP results for relatively soft materials has been questioned [9,10]. Martínez et al. [9] present results of MIP for carbon cloth and carbon paper GDLs. It is stated that carbon cloth GDLs are compressible, while carbon paper GDLs are relatively incompressible. Gieshe [10] discussed that the compressibility of a soft material affects the results of MIP at the high pressures needed to accurately measure samples with small pores. Gieshe, however, does credit MIP for being the only material characterization technique that can simultaneously achieve the pore size distribution, total porosity, skeletal and apparent density, and specific surface area of a sample, and states that pores ranging between 3.5 nm and 500 μm can be investigated with this technique. He also presents that MIP has limitations in addition to compressibility of a soft sample, such as that MIP only measures the largest entrance towards a pore, and not the inner size of a pore, and also that MIP cannot analyze closed pores since mercury has no way of intruding that pore. Despite these actualities, a pore not accessible to mercury is possibly a pore not accessible by the reactants or products in a PEMFC, so these errors resulting from MIP might even aide the accuracy of calculations for liquid transport and gas diffusion through a GDL. In addition, Dehl [11] performed MIP experiments on carbon fiber substrates with a PTFE treatment. The porosity was determined to be 70%, and the samples he tested are very similar to the ones investigated in this experiment. He concluded that MIP can be used on the PTFE–carbon composite without fear of mechanically compressing it.

In using either the SEM or the MIP method of determining porosity, macroscopic pores can be distinguished from microscopic pores, and each affects the performance of a fuel cell differently. The benefit of using the SEM method is that porosity resulting from each material in the GDL is quantified, whereas MIP quantifies the pore size distribution, but does not indicate where in the sample, the pores are located. In a PEMFC, since it is optimal to have smaller pores in a GDL located nearer to the membrane electrode assembly for increased current density [1], it is important to know this, and it will soon become apparent that material interactions within the GDL can skew these results from what one may expect.

Table 1
Modified carbon paper samples to be used as GDLs in PEMFCs.

	Substrate wet proofing	MPL	MPL wet proofing
Sample J	0%	No	N/A
Sample K	10%	Yes	10%
Sample L	40%	Yes	10%
Sample M	40%	Yes	40%

2. Experimental

The samples consisted of Toray TGP-H-060 carbon paper substrates, which were then modified by BASF Fuel Cell, Inc., who treated the substrate with a proprietary polymeric WPM, such as PTFE, in the amount of either 10% or 40% to the carbon fiber substrate which was then coupled with an MPL, also treated with WPM in differing quantities, as shown in Table 1. Although little information was given as to the compositions of the custom made and proprietary final products, untreated TGP-H-060 is reported to have a thickness of 0.19 mm, a bulk density of 0.44 g cm^{-3}, and a porosity of 78% [12]. The WPM is presumably PTFE, and the MPL is presumed to primarily consist of pressed carbon black powder and a binding agent. These GDLs were subjected to numerous tests in addition to porosity measurements. The results of fuel cell performance for these very samples and others, as well as MIP results and pore size distributions obtained from MIP are described by Martínez et al. [8].

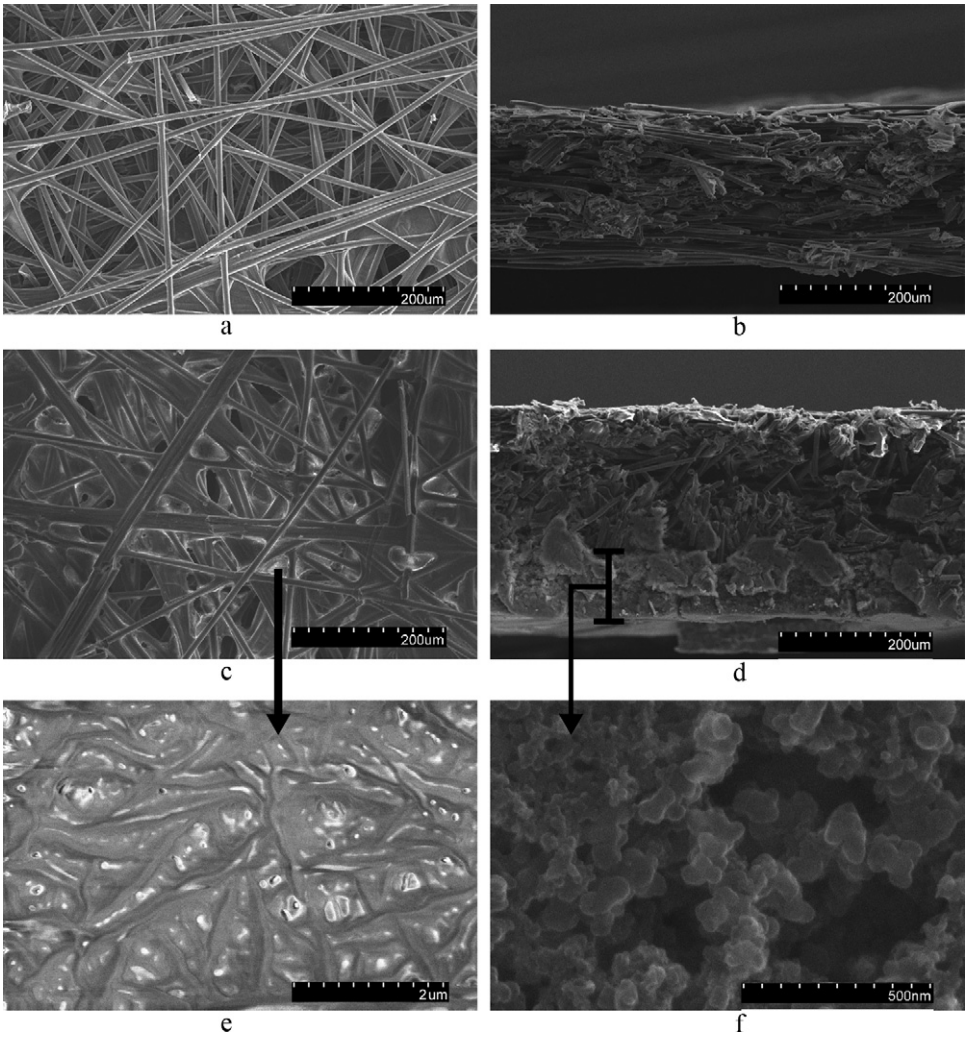

Fig. 1. SEM images of samples J (no WPM, no MPL) and L (heavy WPM, and carbon substrate coupled to MPL). Images shown are of (a) a sample J surface image, (b) sample J edge image, (c) sample L surface image, (d) sample L edge image, (e) a high magnification image of the WPM, and (f) a high magnification image of the MPL.

For this study, samples were analyzed using a Hitachi S-4800 high resolution field emission SEM, operated in secondary electron mode. Images were taken for uncoated samples at an accelerating voltage of 15 keV. The samples were fairly conductive as a whole, and needed no preparation to image the carbon fiber substrate and MPL. Sample surfaces and cross-sections were imaged at a relatively low magnification, initially 200×, whereas detailed structure of the MPL was delineated in much higher magnification images, initially 60 k×–100 k×. The high magnification images were well within the capabilities of the microscope, which has a secondary electron spatial resolution of 1.0 nm at 15 keV [13]. The WPM was not as conductive as the substrate and MPL, so it appeared brighter than the fibers, as was desired in the low magnification images. However, to image the WPM at higher magnifications, countermeasures were needed to combat the effects of localized charging. A sample was gold sputtered for 15 s using a Hummer 6.2 sputtering device, to apply a gold coating with an average thickness on the order of nanometers. The WPM was then imaged at 1.0 keV, initially 20 k× magnification. For each material within a sample, the images were examined to determine the images of each type which are most representative of the sample to be analyzed.

After three to four images of each type were chosen, Adobe Photoshop CS5 [14] was used to set a threshold to the image contrast such as to separate areas of a solid of interest in a known depth from the rest of the image by assigning the pixels in the image as either completely white or completely black. The measurement tool was then used to quantify the number of white pixels which represent the area of the solid of interest. Since the image area is known, the area fraction filled by the solid of interest is calculated, as is ultimately, the volume fraction of solid for each material. The volume fraction of fibers is approximately the area fraction divided by the number of layers examined, where a layer was defined to be a plane with the approximate thickness of the diameter of the carbon fiber. It was not necessary to know the fiber diameter for this calculation to work, but regardless, it was later measured for the purposes of error quantification. Fig. 5b, later shown, provides a visual aide and a simple APL versus volume calculation for stiff, box shaped fibers. As long as the fiber width is equal to the fiber height for these box shaped fibers, then the two volume fraction results are equal if the area of overlap from the fiber intersection is added to the area of fibers before performing the APL quantification. At an intersection between two fibers the thickness of the layer is two fiber diameters; however, since the fibers are fairly flexible, and spacing between the fibers is relatively large in comparison to the fiber diameter, the average thickness for a plane of intersecting fibers is much closer to one fiber diameter. Hence, one plane of intersecting fibers was defined to be a layer. This is different from the image shown in Fig. 5b for rigid fibers, where the thickness of the layer of intersecting fibers is uniformly twice the diameter of the model fibers. For relatively flexible fibers, the thickness of the

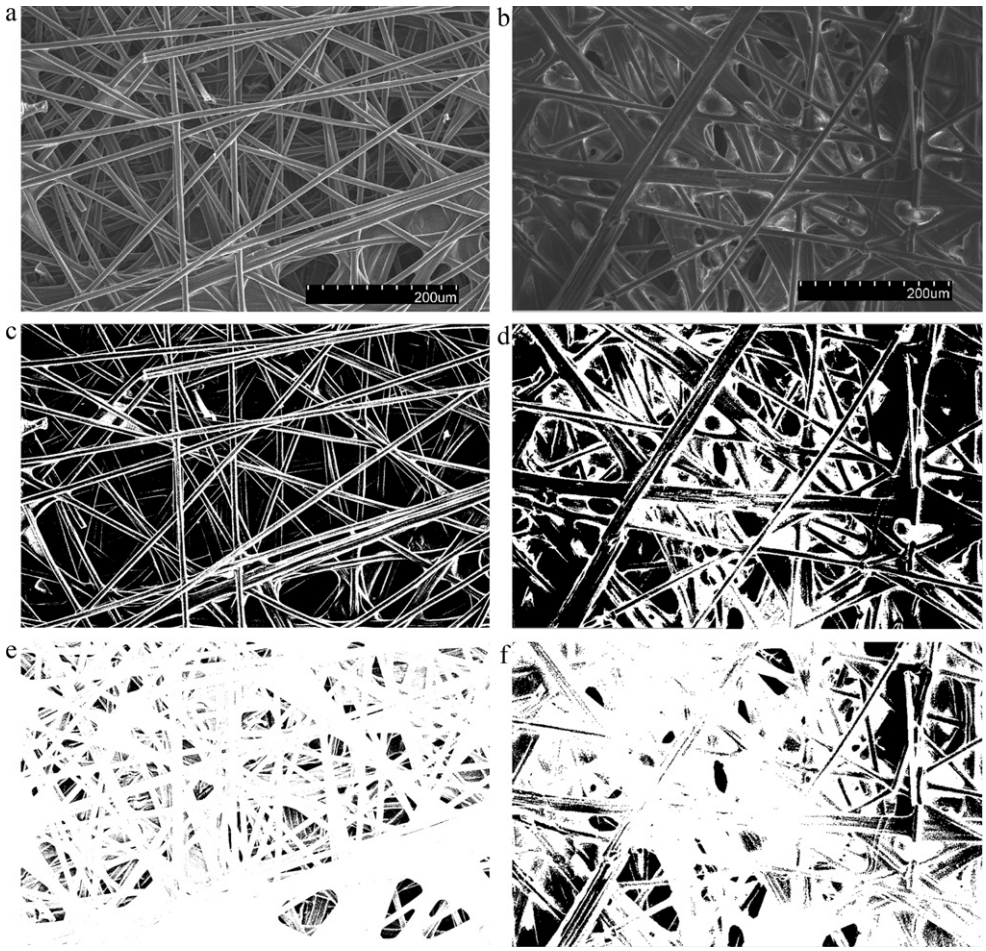

Fig. 2. SEM surface images of (a) sample J and (b) sample L. The remaining images are the thresholded images after step 1 and 2 for sample J where 4 layers were examined, and sample L where only 2.5 layers were examined because of the increased WPM amount. Shown are the thresholded images resulting after step 1 for (c) sample J and (d) sample L, and thresholded images resulting after step 2 for (e) sample J and (f) sample L.

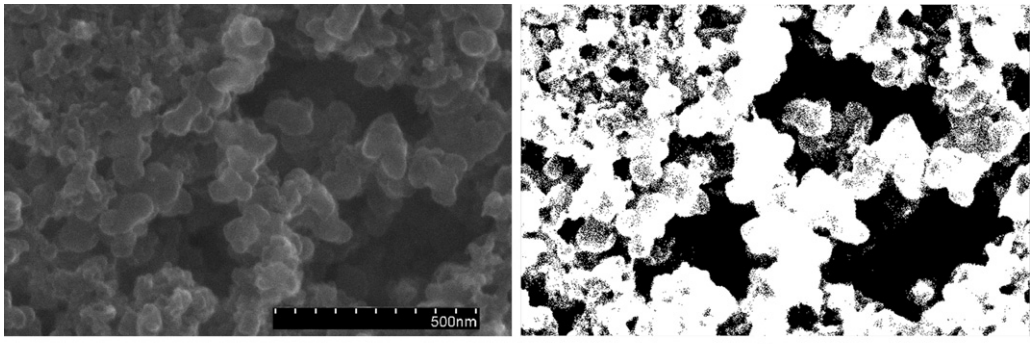

Fig. 3. Sample L MPL images. Shown are (a) a surface image, and (b) an image contrast thresholded to the average diameter of the globules.

layer is two fiber diameters only if fiber intersections lie directly above fiber intersections in the below layers which is an extremely rare case, and most likely accurate for less than 1% of fiber intersections seen in a 2D image. Assuming that the layer thickness of one fiber diameter is accurately assigned, it is also possible to contrast threshold to ½ layer resolution, where ½ of a layer was defined to be a set of non-intersecting fibers in the same plane. Since a layer is defined as a plane of intersecting fibers, intersections were closely examined during the thresholding process. Fibers in the top or first layer were spotted by first finding the top intersections. Fibers in the second layer were found by first finding fiber intersections near top intersections, where only half of the fibers involved in the intersection directly make contact with fibers from the top layer. This method of examining intersections allowed for precise assignment of fibers to certain layers while contrast thresholding.

3. Results and discussion

3.1. Collection of area per layer measurements

The first step of the thresholding technique was to visually separate a given number of layers of the WPM from the fibers and pores. This could be done because the less conductive WPM generally

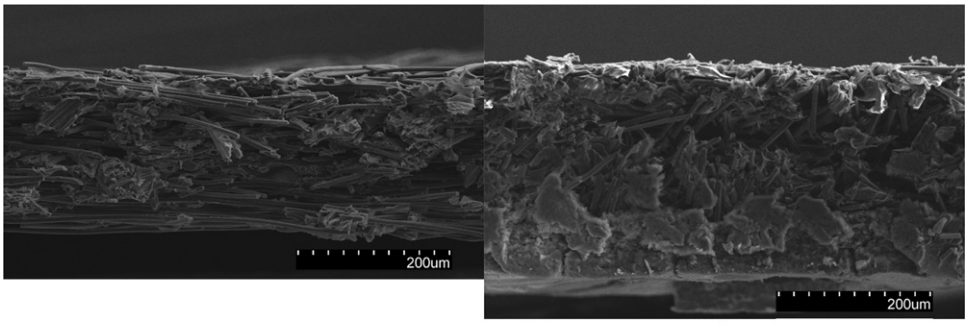

Fig. 4. Edge images of (a) sample J with no MPL and (b) sample L with MPL coupled to the substrate.

appeared brighter than the fibers in the images, and brightness of a layer decreased as the depth of the layer from the surface increased because a weaker signal reached the detector from these layers. The fibers were used to reference the layer where the WPM resides. The WPM strongly bonded to the fibers, existed primarily as bonding material between fibers, and was fairly uniformly distributed between layers. The WPM was assigned to the corresponding layers of the fibers it bonded to so that intensity thresholding could be used to exclude WPM residing in layers beneath the given number of layers examined, by assigning the corresponding pixels black. Sample J had no WPM, but there was still evidence of a second material other than fibers, which was used to bind the fibers. Although this substance is not WPM, it is polymeric as is the WPM and is treated as WPM for porosity calculations. The white pixels, representing the area of the 2D image filled by the WPM and/or binder within the depth examined, were counted using the Adobe Photoshop measuring tool. The resulting measurements after each step are shown in Table 3.

The second step was to threshold to the same number of layers for the sample, but so that both carbon fibers and the WPM were shown as white and pixels counted, where as the pores were left black. Fig. 2 shows the images resulting from step 1 and 2. After subtracting the image area resulting from step 1 from that of step 2, the image area fraction filled by fibers was found, as is shown in Table 3.

In step 3, we determined area fraction of solid to be used in calculating micro porosities. For the MPL, high magnification images are thresholded so that the depth of field seen is approximately the diameter of the polymer globules. Again, Adobe Photoshop is used to count the fraction of white to black pixels, to determine the area filled by solid. The WPM image was not used quantitatively, only qualitatively. Examination of the WPM in Fig. 1e shows that although there is a small porosity, the pores are certainly closed. For this reason the WPM is treated as though it were completely solid for the purposes of MacMullin number calculation, as these pores can neither be intruded by mercury, nor the reactants and products of the PEMFC. Images of the MPL resulting from step 3 are shown for sample L in Fig. 3.

Since the MPL was coupled to the fiber substrate without much overlap as opposed to a uniform distribution throughout the sample, edge images were used to measure the thickness of the substrate, and the thickness of the MPL in step 4. This allowed for a ratio of MPL thickness to that of the substrate to be found and used in calculating the overall porosity. Fig. 4 shows the difference in thickness that the MPL adds to the GDL.

3.2. 3.2Geometrical and statistical adjustments to convert area fractions into volume fractions

Now the raw data has been obtained, but several geometrical approximations and statistical adjustments need to be made before the volume fractions of solid can be found for each material, in step 5. Beginning with the fibers, the solid volume fraction is the area fraction of solid divided by the number of layers examined after two inaccuracies are accounted for. The error due to the inability to account for the cylindrical shape of the fibers using the 2D technique (the first error), and the error due to volume hidden by overlapping strands (the second error) can both be quantified. In Fig. 5b, there is shown two long, stretched out boxes, which overlap. When examining a 2D surface image of carbon fibers from above, it would be impossible to tell whether these shapes where boxes at all, or whether they were cylinders. Assuming the shapes were boxes, the area fraction of the boxes in the surface image is known, and height of the boxes are known, and the volume fraction of the boxes can be approximated by the area fraction of the boxes multiplied by the fraction of length that each box fills in the z-direction, leaving only the second error to be accounted for. However, since it is known that the shapes are cylinders and not boxes, the volume fraction of solid is overestimated by the ratio of the volume of the box, with a width of $2r$ and length L, to the volume of a cylinder, with a radius, r, and length, L, as depicted in Fig. 5a.

To calculate the second error, the area hidden by a fiber intersection was quantified for all whole number intersection angles from 0° to 90°. The area hidden by a fiber intersection is a function of the fiber diameter and angle of intersection found by:

$$A_i = \frac{d_f^2}{\sin(\theta_i)} \tag{5}$$

where A_i is the area hidden by a single intersection, d_f is the fiber diameter, and θ_i is the angle of intersection. The average and standard deviation of the intersection angles was then found by measuring the acute angles of several intersections in a single layer, and recording the supplementary angles as additional measurements. From this, the probability density function of intersection angles was determined as shown in Fig. 6, and the weighted average area hidden by an intersection between two fibers was found by multiplying the results of each intersection area determined in Eq. (5) with the probability of intersecting at that angle, or the supplementary angle shown in Fig. 6, and taking the average of the results. The number of intersections in a layer was determined for a known area by editing a surface image so that only 1 layer was visible. Intersections in this image were manually counted and compared to a surface image edited so that 1.5 layers were seen. Adding the additional half layer in this case almost exactly tripled the number of intersections counted, as this doubles the half layers above the lowermost half layer examined, of which intersections are added to intersections from the top two half layers. Adding an additional half layer would hence triple the half layers above the bottom one, so it is expected that this would increase the number of intersections counted sixfold (1 + 2 + 3) from the intersections counted for just two half layers. This relationship was used to find the area hidden in a half layer by the half layers above it. The area hidden in

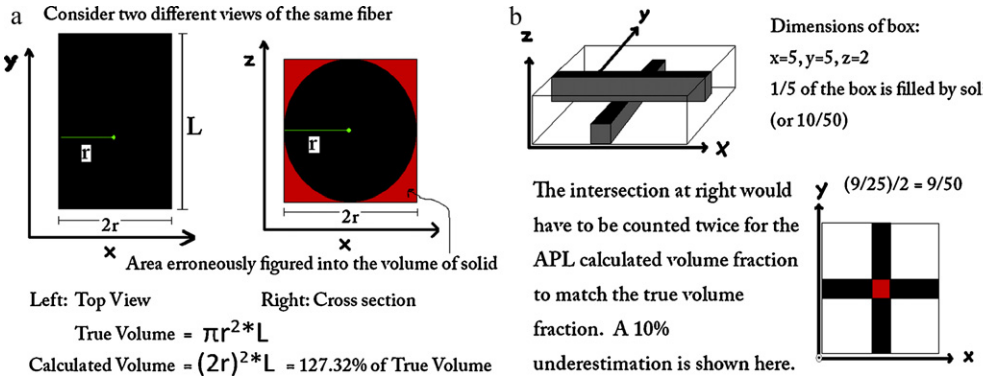

Fig. 5. Diagrams pertaining to (a) the first error, and (b) the second one.

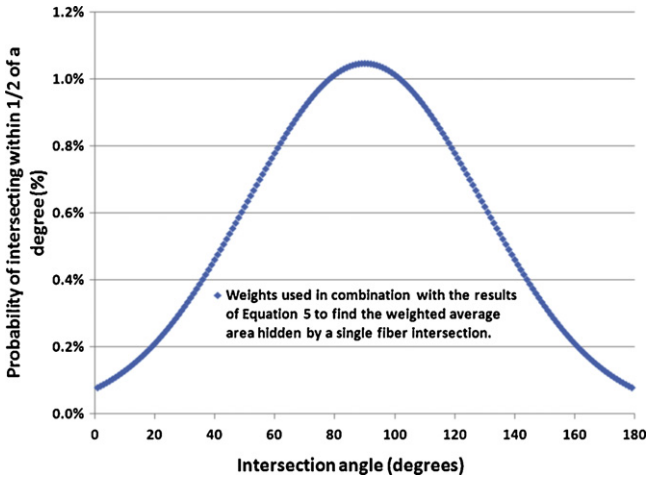

Fig. 6. A graph of the probability density function of intersection angles, determined by the standard deviation of the measured angles.

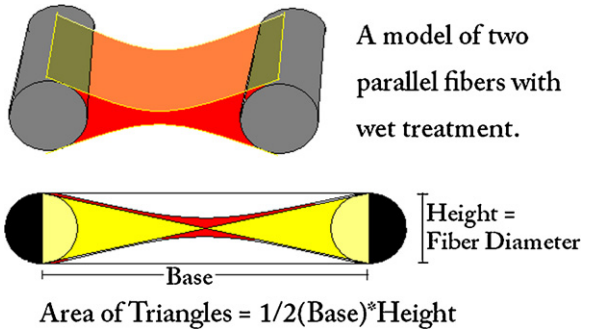

Fig. 7. A 3D model and cross-section of WPM bonded to fibers.

a half layer by the half layer above, A_L, is the count of intersections, multiplied by the weighted average intersection area. The total area hidden in a half layer, A_T, by all intersections above for a given number of half layers, N, is shown with:

$$A_T = \sum_{i=1}^{N} [A_L(i-1)] \tag{6}$$

Finally, with this information, the cumulative area hidden in all half layers by intersections with all half layers above, A_C, is simply the sum of A_T calculated for each half layer:

$$A_C = \sum_{i=1}^{N} (A_{T(i)}) \tag{7}$$

Percentage of area hidden by intersections with above layers was then calculated based on a percentage of image area. Results of these calculations are displayed in Table 2 for up to six layers. The fiber volume fraction is then found by first adding the area, A_C, found as a percentage of image area, to the measured fiber area, recalculating the area fraction per layer examined, and finally adjusting this result for the first error. After accounting for these two errors, the porosity calculated by SEM for sample J, which had no wet proofing or MPL, fell between the result of 78% measured by the manufacturer, and the result of 80% found by MIP, as shown in Table 3.

The wet proofing exhibited a behavior similar to the image in Fig. 7. Only a fraction of the layer thickness was filled by the polymer. The treatment bonded to the fibers, and hence the polymer was thickest near the fibers. As distance was increased from the fibers, the polymer layer would thin to almost non-existence in the center. Because of this, the cross-section thinning was approximated by triangles for samples treated with WPM. Although this estimation is not exact, the triangles underestimate in some areas and overestimate in others, so the approximation is not too far off. The area fraction to volume fraction conversion coefficient for the WPM was crudely approximated to be one half, meaning that the measured area of WPM in a layer only half filled the volume. What mainly makes this a crude approximation is that this conversion coefficient is not accurate for all amounts of wet proofing. For example, if the substrate is completely saturated with WPM, than the fraction of the layer filled by this polymer will be much closer to one. Also, for WPM amounts greater than 50% of the saturated amount, it would be impossible to say that this amount only half fills a layer. Likewise, if very light wet proofing is applied, such that the WPM amount is not enough to bridge the spacing between fibers, then the conversion coefficient is again inaccurate, and in the most extreme case (if no gaps are bridged) it will be slightly greater than one, because a large percentage of the WPM will not be seen as it is hidden underneath the fibers. In the latter case, however, since the WPM amount is small, so is the error involved with the use of this coefficient, which only differs for sample J (no wet treatment), where no volume correction is needed, and the coefficient is assumed to be one. For the other samples used in this experiment, which had wet treatments in the amount of either 10% or 40%, it is assumed that the WPM behaves as shown in Fig. 8, because of the strong bonding of the WPM to the fibers. Differing WPM amounts in this range will primarily affect the WPM areas measured in the surface image, although this is fairly inexact for small amounts as is evident by the equal calculation of WPM/binder amounts shown in Table 3 for samples J and K. This should not be the case, but although the WPM for these two samples likely fill a fraction between one

Table 2
Quantification of the area hidden by fiber intersections for a given number of layers.

Area of image (μm^2)	1,044,204
Weighted average error per intersection (μm^2)	60
Count of fiber intersections in the top layer	86
Average area of error for the top layer, A_L, (μm^2)	5177

Half layers, N	Total error for the half layer, A_T (μm^2)	Cumulative error, A_C (μm^2)	A_C as a percentage of image area
1	0	0	0.00%
2	5177	5177	0.50%
3	10,354	15,532	1.49%
4	15,532	31,063	2.97%
5	20,709	51,772	4.96%
6	25,886	77,658	7.44%
7	31,063	108,721	10.41%
8	36,240	144,961	13.88%
9	41,417	186,378	17.85%
10	46,595	232,973	22.31%
11	51,772	284,744	27.27%
12	56,949	341,693	32.72%

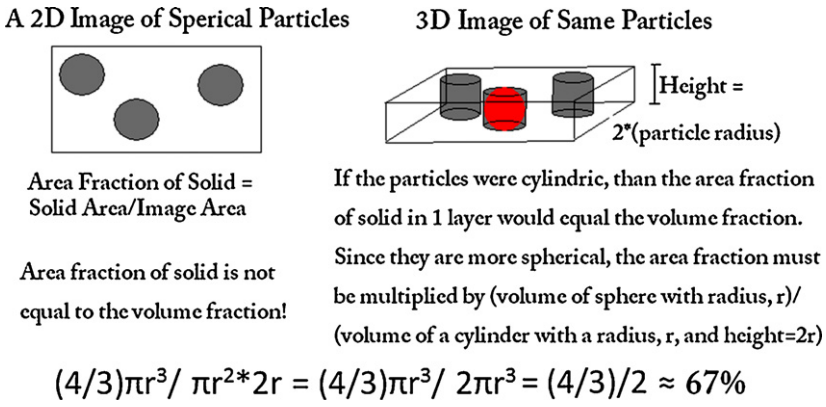

Fig. 8. A diagram explaining the conversion coefficient needed to convert the area fraction of circular particles in a 2D image into a volume fraction for spherical particulates.

half and one, they have the least wet proofing so are not hugely affected by this inaccuracy.

For the MPL, if the area fraction per layer were to be considered a volume fraction, it would be correct assuming that the polymer globules were actually cylinders instead of spherical. Fig. 8 shows a representation of 2D and 3D images of spherical particles. In using the APL technique on 2D images, the curvature normal to the plane of the image is not seen. The area fraction of a single layer is equivalent to the volume fraction if there is no curvature in this dimension, which is to say that cylindrical volumes are calculated for spheres. To correct this, the area fraction is multiplied by the ratio of (the volume of a sphere with radius r/the volume of a cylinder with height, h, equal to $2r$) to convert to the volume fraction of spheres. This ratio turns out to be about 67%, but it might be a slight overestimate of porosity since many of the globules are agglomerated together.

3.3. Analysis of results and error

After step 5, the volume fractions of each material are calculated. Fig. 9 shows a graph of the cumulative pore volume as measured by MIP by Martínez et al. [8]. The overall porosities are additionally shown in Table 3. In comparing the results of the porosities calculated by SEM to those measured by MIP, it was found that there was little discrepancy between the two techniques. The perceived accuracy of the results, rounded to two significant figures for both techniques, was completely unexpected for the samples with WPM and MPL as there are numerous errors that went unaccounted for in the SEM analysis. It is unknown as to whether the APL technique should overestimate or underestimate the porosities of these GDLs, because these errors seem to work against each other. In addition to the mentioned overestimation of MPL porosity with this technique, two more errors which would also result in the overestimation of porosity for the GDLs with WPM and MPL can be explained. One is the error relating to the lack of quantification of area hidden by the WPM, which is hard to quantify assuming that the WPM amounts are not initially known to those using this method. This error is similar to the 2nd error described in Section 3.2, for which the fiber areas are underestimated, except it is the WPM that hides

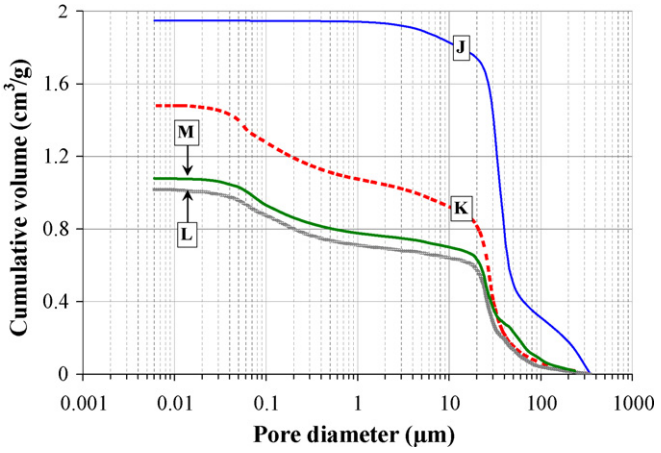

Fig. 9. Cumulative pore volume, as determined by MIP by Martínez et al. [8].

Table 3
Results of the porosities calculated by SEM and measured by MIP for four carbon paper GDLs.

			Sample J	Sample K	Sample L	Sample M
Layers thresholded for steps 1 and 2			4	2.5	2.5	2
Average image area for steps 1 and 2 (pixels)[a]			1,068,160	1,065,280	1,068,160	1,066,667
Step 1:	Average measured area of WPM (pixels, 4 images)		324,908	362,938	466,815	650,233
	Average area fraction of wet treatment + substrate binder		0.28	0.34	0.44	0.61
	Average area fraction of wet treatment/layer		0.07	0.14	0.17	0.31
Step 2	Average measured area of fibers and WPM (pixels, 4 images)		950,502	787,302	927,566	953,986
	Average area fraction of fibers		0.58	0.40	0.43	0.26
	Average area fraction of fibers/layer		0.15	0.16	0.17	0.13
Step 3	Average measured area for one layer of MPL (pixels, 3 images)		0	551,819	644,782	605,713
	Average MPL image area (pixels)[a]		NA[−1]	1,066,667	1,064,960	1,067,520
	Average area fraction of solid in MPL		NA[−1]	0.52	0.61	0.57
Step 4	Average MPL thickness (μm, 30 measurements, 3 images)		0	87	112	128
	Standard deviation in MPL thickness (μm)		0	28	21	16
	Average GDL thickness (μm, 30 measurements, 3 images)		211	303	275	295
	Standard deviation in MPL thickness (μm)		11	11	22	11
	Average fraction of MPL/GDL thickness		0	0.29	0.41	0.43
Step 5:	Volume overestimation by not Accounting for cylindrical shape of fibers (1st error)		27.32%	27.32%	27.32%	27.32%
	Image% of solid area underestimation due to overlapping fibers calculation (2nd error):	Fiber diameter (measured, μm):	6.1	6.1	6.1	6.1
		Standard deviation of intersecting angles (rad):	0.68	0.68	0.68	0.68
		Weighted average area hidden by a fiber intersection (Eq. (5), μm²)	60	60	60	60
		Count of intersections/1 layer @ 200×	86	86	86	86
		Total solid area hidden by fiber intersections for the given number of layers examined (Eq. (7) and Table 2, μm²)	144,961	51,772	51,772	31,063
		Image area (μm²)	1,044,204	1,044,204	1,044,204	1,044,204
		% of solid image area hidden by fiber intersections (Table 2):	14%	5%	5%	3%
	Average fiber volume fraction (error adjusted):		0.14	0.14	0.15	0.13
	Overall error correction to fiber volume fraction (1st and 2nd errors)		−3%	−11%	−12%	−4%
	Fraction of layer filled by WPM:		1	1/2	1/2	1/2
	Average volume fraction of wet treatment:		0.07	0.07	0.09	0.15
	2D → 3D coefficient for MPL error adjustment:		NA[−1]	2/3	2/3	2/3
	Average volume fraction of solid in MPL:		NA[−1]	0.34	0.40	0.38
Total porosity calculation:						
Volume fraction of substrate (fibers + WPM):			0.21	0.21	0.24	0.28
Volume fraction of solid in MPL (microlayer):			NA[−1]	0.34	0.40	0.38
Fraction of MPL/GDL thicknesses:			0	0.29	0.41	0.43
Volume fraction of solid:			0.21	0.25	0.31	0.32
Porosity by scanning electron microscopy			79%	75%	69%	68%
Porosity by mercury intrusion porosimetry [8][b]			80%	75%	68%	69%

[a] Image areas are not all the same because the scale bars were cropped out of the images before thresholding.
[b] Samples J, K, L and M are listed as samples 1, 3, 6 and 7 (respectively) by Martínez et al. [8].

information in the below layers which are assumed through the calculations to be pores. To reduce the effects of this cause for error, fewer layers were examined for samples with a large amount of WPM, but this also reduced the volume analyzed in the sample, and did not completely nullify the error. This might explain the lower fiber volume versus WPM volume amounts calculated for sample M. For sample J, where the actual WPM amount is zero, but a small binder amount is treated as if it were WPM, this error is extremely small. Another known error is the lack of quantification of overlap between the MPL and substrate, which is assumed by the calculations to be zero. Adjusting for this error should cause for a reduction of porosity measured for all samples with WPM, i.e. samples K, L and M. This error should be quite minimal as the small region of overlap has macro pores in the substrate filled by MPL measured to be 60–66% porous, depending on the sample. However, it is not certain that this is the case. The MPL was imaged at high magnifications, and these images were used to calculate the porosity of the MPL. Martínez et al. [8] discuss cracking in the MPL, and in one image, a crack with a separation of 32 μm is shown. Cracks in the MPL not seen in high magnification images could cause for the APL technique to underestimate the MPL porosity by as much as 5%. An additional cause for a porosity underestimate in this technique was discussed at the end of Section 2. The average thickness of a layer was estimated to be one fiber diameter, however when the intersections between fibers in one layer lay directly above intersections in a layer below, the thickness of the layer at that point is two fiber diameters. Since this is an extremely rare case, this error is fairly small, and a significant deviation from the estimated layer

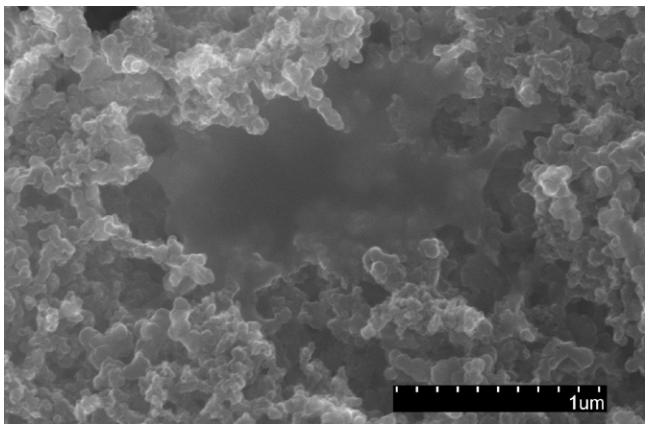

Fig. 10. High magnification image of MPL for sample M. This is the largest pore noticed in the high magnification SEM images of the MPL for all samples.

thickness would certainly be noticed in sample J. This sample is either completely unaffected or only negligibly affected by any of the above mentioned errors.

In examining high magnification images of the MPL, such as the one shown in Fig. 3, it can be seen that micro pores in this layer can have diameters as large as 500 nm. In a single case, a pore with a diameter slightly larger than 1 μm was noticed in the high magnification MPL images, and is shown in Fig. 10. This correlates quite well to the graph of the cumulative pore volume determined by MIP in Fig. 9. It can be seen in Fig. 9 that an inflection point exists at approximately 1 μm (perhaps 2) for the samples with bimodal pore distributions, samples K, L and M. In addition, the percentage of pores with a diameter less than 1 μm is determined to be approximately 28%, 30%, and 30% respectively, for these samples. When considering the expected effects of wet treatment to the MPL, such as the reduction of porosity and increased thickness of the layer with increased wet proofing, these results also correlate well with the fraction of MPL/GDL results determined by thickness measurements in step 4 reported in Table 3. A complete breakdown of material and pore volumes is shown for each sample in Fig. 11. Additionally, for samples with MPL, a volume percentage of macro pores and micro pores are shown for comparison with the results obtained by MIP. The percentage of micro pores determined by SEM were about 25%, 35% and 40% respectively, for samples K, L and M. The breakdown of sample M in particular, showed a higher percentage of micro pores than were determined by MIP. The measurements by MIP should be more accurate than the calculations by SEM if the MPL is relatively incompressible as was determined for the substrate; however if this is not the case, then the percentage of micro pores will be underestimated by MIP. Interestingly enough, the porosity of the MPL determined by SEM did not vary significantly with respect to WPM amounts in the MPL, and there was certainly no correlation seen in the MPL porosities. This is backed by the results obtained by MIP, which show that additional wet proofing to the MPL did not reduce the porosity of the GDL. In fact, the results for samples L and M suggest that additional wet proofing to the MPL slightly increased the porosity of the GDL. Instead of a

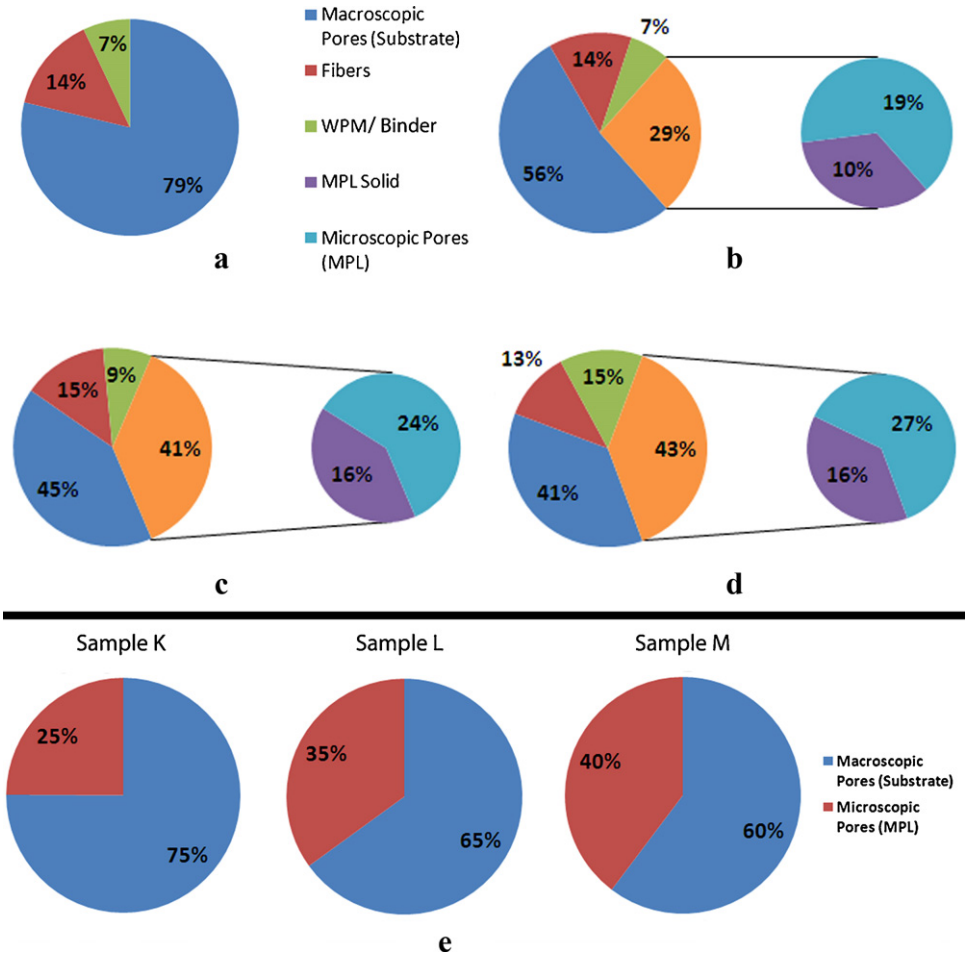

Fig. 11. Sample breakdown of materials and pores by volume for (a) sample J, (b) sample K, (c) sample L, and (d) sample M. Pore volume percentages are shown (e) for the samples with MPL.

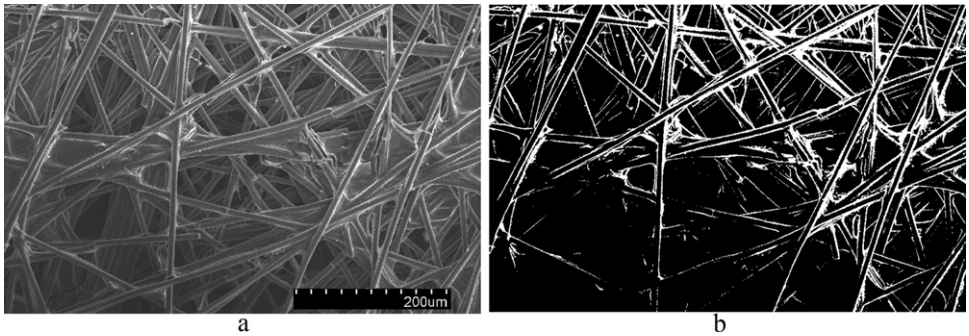

Fig. 12. Surface images of sample K (a) unthresholded, and (b) contrast threshold applied in attempt to highlight the WPM.

porosity difference, an increase in thickness of the MPL was noticed by SEM that did seem to correlate to the total WPM amounts in the entire GDL, not just the MPL. While it was initially thought that WPM may have been confused for MPL in thickness measurements, these images were double checked, and the texture of the MPL is quite distinguishable from the WPM even at relatively low magnifications. Another error can be caused in cutting the samples for cross sectional analysis, if the MPL is smeared, pressed into the substrate, or lengthened in the process. It seems less likely that this discrepancy was caused by this error and that there may be a real physical difference in MPL thicknesses between these samples. One possible explanation for the difference in percentage of micro pores calculated for each of the two techniques is the mixing of WPM and MPL at the substrate/MPL interface, resulting in a blend appearing to be purely MPL. This explanation is supported by the total GDL thickness measurements shown in Table 3, which show that samples L and M are slightly thinner than sample K, despite the thicker MPL. From these results, it appears WPM in the substrate tends to "suck in" the MPL, but this appearance could still be attributed to the cutting of the sample if the degree of MPL smearing or dimensional changes were somehow correlated to the wet proofing of the GDL.

Although numerous errors have already been discussed, the APL technique is also subject to human error. Human error can also result since the number of layers has to be precisely thresholded to achieve a reasonable degree of accuracy. Deciding on a number of layers to threshold as well as using the actual number of layers thresholded in calculations is critical. Human error could be removed from the equation by programming Adobe Photoshop or another program to do the thresholding and calculations. If the SEM operator is skilled enough so that the same SEM settings, such as accelerating voltage, probe current, magnification, working distance, and brightness and contrast are used for the same sample type, then theoretically an image thresholded to a given number of layers on a sample will, on average, threshold to the same number of layers on another sample of the same type if the same numerical threshold level is applied. The threshold level still needs to be determined by eye through a calibration, but the benefit is that this allows for a large number of samples to be quickly analyzed or recalculated, which reduces the variance associated with examining very small image areas. Although use of a program should greatly improve speed and accuracy, additional errors can result from less than ideal SEM settings.

One such error is shown in Fig. 12, where the surface image used to evaluate this sample is shown along with a thresholded image to highlight the WPM. It's not so apparent in the unedited image, but it can be seen that the layer does not threshold evenly. This was the case because the image was taken with a misaligned SEM aperture, which caused for an underestimation of the WPM amount. This error could have been easily avoided by choosing a different surface image, so it is a result of human error. This error, however, did not significantly affect the results of sample K because the APL measurements were obtained from four images and averaged to achieve the final results.

Lastly, because one method to reduce the overestimation of porosity for a sample with a high WPM amount is to examine a fewer number of layers, a large sample volume is unable to be analyzed for those samples with this 2D technique, and that volume may not be representative of the sample. Even if a large number of images are used to collect measurements, the penetration depth will be quite shallow and the absolute top layer or half layer may contain a lower WPM amount than below layers, for instance. The APL technique was designed to analyze very porous samples. Other methods, such as the method of measuring pore radii or dimensions may yield more accurate results for samples less than 50% porous.

4. Conclusion

The APL method was developed to determine the 3D porosities of carbon paper GDLs for the purpose of MacMullin number calculation, and will work for similar samples with a high porosity. The higher the porosity of the sample, the more accurate the method is. The difference between SEM calculated porosities and MIP measured porosities were less than 2% in the worst case. The four samples appear to be drastically different at low magnifications, but porosity analysis by SEM shows an absolute porosity difference of only 11% from the untreated carbon paper to the most heavily treated sample, which may be surprising. This is because the apparent difference in the MPL amounts are less extreme than it appears when the porosity at high magnification is considered, and WPM areas seen in the surface images are reduced by half because this material only half fills a layer on average.

The image processing technique not only allows for the GDL porosity to be calculated, but it distinguishes between macroscopic pores and microscopic pores, and allows for a complete sample breakdown of materials and pores by volume. MIP results correlated well with the porosity and pore size distribution analyzed by SEM, adding confidence to the accuracy of results for both methods. In a PEMFC, it has been shown that smaller pores nearer to the membrane electrode assembly increase the current density in the electrode. Hence, knowing the thickness of the MPL, and its distribution are important benefits provided by SEM that are not by MIP. Porosity analysis in this fashion can add information as to the whereabouts and character of pores, cracks, and hydrophobic materials in a GDL, which leads to a better understanding, and ultimately, optimization of GDLs for PEMFCs.

Acknowledgement

This research was supported by the National Science Foundation of Industrial/University Collaborative Research Center for Fuel Cells, by NSF grant EEC-0324260.

References

[1] S. Shimpalee, U. Beuscher, J.W. Van Zee, J. Power Sources 163 (2006) 480–489.
[2] M.J. Martínez, S. Shimpalee, J.W. Van Zee, J. Electrochem. Soc. 156 (1) (2009) B80–B85.
[3] M.J. Martínez, S. Shimpalee, C. Tong, M. Ohashi, J.W. Van Zee, ECS Trans. 25 (1) (2009) 357–367.
[4] Z. Yu, R.N. Carter, ECS Trans. 19 (17) (2009) 1–15.
[5] C. Igathinathane, L.O. Pordesimo, E.P. Columbus, W.D. Batchelor, S.R. Methuku, Comput. Electron. Agric. 63 (2008) 168–182.
[6] R. Diego, J. Estelles, J. Sanz, J. Garcia-Aznar, J. Biomed. Mater. Res. B: Appl. Biomater. 81B (2007) 448–455.
[7] G. He, Z. Zhao, P. Ming, A. Abuliti, C. Yin, J. Power Sources 163 (2007) 846–852.
[8] M.J. Martínez-Rodríguez, C. Tong, S. Shimpalee, J.W. Van Zee, ECS Trans. 33 (1) (2010) 1133.
[9] M.J. Martínez, S. Shimpalee, J.W. Van Zee, J. Electrochem. Soc. 156 (5) (2009) B558–B564.
[10] H. Gieshe, Part. Part. Syst. Charact. 23 (2006) 9–19.
[11] R.E. Dehl, J. Biomed. Mater. Res. 16 (5) (1982) 715–719.
[12] Toray TGP-H Specifications, http://www.fuelcell.com/techsheets/TORAY-TGP-H.pdf, 08/2011.
[13] University Spectroscopy and Imaging Facilities website, http://usif.arizona.edu/equipment/s4800.html, 05/2011.
[14] Adobe Photoshop CS5, www.adobe.com/products/photoshopextended.html, 05/2011.